Development of a reduced model for energetic particle transport by sawteeth in tokamaks

M. Podestà, M. Gorelenkova, N. N. Gorelenkov, R. B. White,

P. J. Bonofiglo, F. M. Poli, A. Teplukhina and J. Yang

Princeton Plasma Physics Laboratory, Princeton NJ 08543 - USA

M. Cecconello

Department of Physics and Astronomy, Uppsala University, Uppsala, Sweden

M. Vallar

Ecole Polytechnique Fédérale de Lausanne,

Swiss Plasma Center, CH-1015 Lausanne, Switzerland

(Dated: October 19, 2021)

Abstract

The sawtooth instability is known for inducing transport and loss of energetic particles (EP), and for generating seed magnetic islands that can trigger tearing modes. Both effects degrade the overall plasma performance. Several theories and numerical models have been previously developed to quantify the expected EP transport caused by sawteeth, with various degrees of sophistication to differentiate the response of EPs at different energies and on different orbits (e.g. passing vs. trapped), although the analysis is frequently limited to a single time slice during a tokamak discharge. This work describes the development and initial benchmark of a framework that enables a reduced model for EP transport by sawteeth retaining the full EP phase-space information. The model, implemented in the ORBIT hamiltonian particle-following code, can be used either as a standalone post-processor taking input data from codes such as TRANSP, or as a pre-processor to compute transport coefficients that can be fed back to TRANSP for time-dependent simulations including the effects of sawteeth on energetic particles. The advantage of the latter approach is that the evolution of the EP distribution can be simulated quantitatively for sawtoothing discharges, thus enabling a more accurate modeling of sources, sinks and overall transport properties of EP and thermal plasma species for comprehensive physics studies that require detailed information of the fast-ion distribution function and its evolution over time.

PACS numbers:

I. INTRODUCTION

The ability to predict the evolution of tokamak discharges is critical for the success and controllability of future fusion reactors. For steady-state reactors mostly relying on self-sustained plasma heating by fusion products (i.e. alpha particles), predictions need to be able to account for possible off-normal events such as the appearance of plasma instabilities, so that appropriate control strategies can be devised to steer the plasma state towards more stable conditions and to avoid the termination of the discharge.

Internal kinks are one of the many instabilities that can dramatically affect the evolution of a tokamak discharge, e.g. by suddenly redistributing thermal plasma and fusion products in so-called *sawtooth* crashes. Abundant literature exists that describes the sawtooth phenomenology either based on experimental data (see e.g. [1][2][3][4][5]) or based on theory and modeling results [6][7][8][9][10], including discording conclusions on main features of the sawtooth cycle (see e.g. [5][11][12] and references therein). This work does not attempt to solve open issues regarding the specific physics of sawteeth. Instead, it focuses on the main effects of sawteeth on energetic particle (EP) transport and loss, and how those effects can be incorporated in numerical codes for integrated tokamak simulations. In the following, it is assumed that sawteeth result in periodic crashes of the core plasma when the q-profile drops below unity, followed by a flattening of the safety factor to $q \approx 1$ inside the $q = 1$ radius [6][8]. This picture is qualitatively consistent with the Kadomtsev model implemented in the tokamak transport code TRANSP [13] that is broadly used for simulations of tokamak discharges.

A general feature of sawtoothing plasmas is the evidence of an explosive growth of an internal kink with a dominant $(n, m) = (1, 1)$ component, where n and m are the toroidal and poloidal mode numbers, respectively. Energetic particles are affected by the instability, causing their redistribution and, possibly, loss from the core plasma region. Two main EP transport mechanisms have been identified, namely (i) non-resonant transport of particles that tend to follow the evolution of the perturbed magnetic field lines during a sawtooth crash [8][14], and (ii) resonant transport [15]. Criteria for which EPs are subject to the first mechanism have been derived in terms of a *critical energy* for co-passing and trapped fast particles [14], suggesting that trapped fusion products - experiencing large orbit drifts across magnetic surfaces - are expected to be mostly immune from non-resonant transport. Resonances between EPs and the $(1, 1)$ mode can, however, still induce significant transport of fusion products [15][16][9][17]. Therefore, simulations of burning plasmas need to take those effects into account, especially when modifications of the distribution function

of fast ions are also relevant to determine the stability of other instabilities such as Alfvénic modes [18], or the mode can serve as a seed for magnetic islands that can trigger tearing modes [19] and eventually lead to a disruption. In addition, modifications of the fast-ion distribution are also important for a quantitative comparison between fast-ion diagnostic data and modeling results [2][20][21][17][22][23][24].

Spherical tokamaks such as NSTX-U [25] provide a good testbed to validate models for EP transport. Due to the low magnetic field, $B_0 \lesssim 1$ T, and highly energetic EPs generated through Neutral Beam (NB) injection with energies $E_{inj} = 60 - 90$ keV, energetic particles experience large orbit drifts across magnetic surfaces, thus mimicking the behavior of fusion products in fusion devices. For the parameters considered in this work (see Sec. II), estimates of the critical energy are $E_{crit} \approx 30$ keV for trapped particles and $E_{crit} \gg 70$ keV (where $E_{inj} = 70$ keV for this scenario) for passing particles [22][23], thus a fraction of trapped particles and most passing particles are expected to be redistributed. However, resonant and non-resonant mechanisms can compete [26] and alter the simple interpretation based on E_{crit} alone.

This work extends previous studies on NSTX-U [22][23] by combining analysis steps for sawtoothing scenarios into a single framework. Models for the mode amplitude evolution, radial mode structure and wave-particle interaction are combined in the Hamiltonian particle-following code ORBIT [27]. The code has been modified to streamline the exchange of input/output files with the NUBEAM module of TRANSP [13][28][29][30] and with other fast-ion analysis codes such as FIDASIM [31].

ORBIT is used for simulations of single sawtooth events, based on a fixed (pre-crash) equilibrium and a realistic fast-ion distribution from NUBEAM. While single time-slice simulations are useful for a quick analysis and for extensive scans of mode parameters (e.g. amplitude, mode structure), the code can also generate an energetic particle transport probability matrix used by the EP *kick model* [32][33] in TRANSP/NUBEAM for time dependent simulations of an entire discharge. Thus, these tools combined provide a comprehensive analysis suite for EP transport by sawteeth that includes the effects of EP transport and loss on the evolution of sources and sinks in TRANSP. The latter - and the inclusion of collisional processes, neglected in ORBIT - are required for additional analysis of thermal transport and MHD stability not limited to sawtoothing scenarios. For instance, understanding the interplay between sawteeth and Alfvénic modes such as that reported in Ref. [18] requires an accurate, quantitative knowledge of the time evolution of the energetic particle distribution. Those scenarios can be expected to be quite common in future burning plasmas.

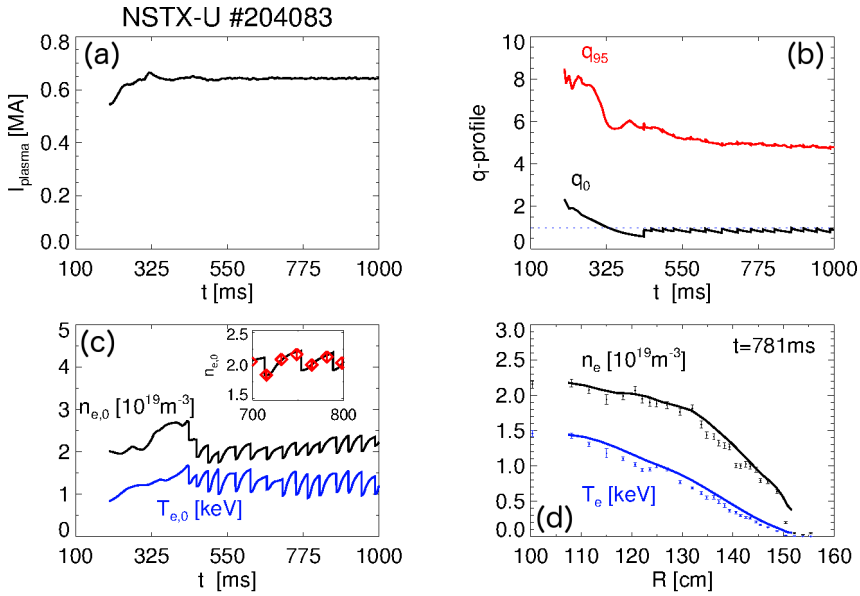

FIG. 1: Summary of the experimental scenario used for this work, NSTX-U discharge #204083. (a) Plasma current. (b) Safety factor on axis, q_0, and at the plasma edge, q_{95}, as computed by TRANSP. (c) Evolution of central electron density and temperature as reconstructed through conditional sampling over sawtooth cycles. The inset compares the reconstructed density (black line) with the raw data (red symbols). (d) Electron density and temperature profiles at the time of interest as measured by Thomson scattering (symbols) and reconstructed through conditional averaging (solid lines).

The development of the framework and initial tests based on a reference NSTX-U discharge are discussed in the remainder of this work. The extension to other devices and the validation against more experimental data are left for future publications. The reference NSTX-U scenario used for this work is introduced in Sec. II. Section III begins with an overview of the workflow that has been developed for the analysis of fast ion transport by sawteeth, followed by more detailed descriptions of the different elements composing the workflow. An example of stand-alone analysis through ORBIT is discussed in Sec. IV. The example is also used to test some of the hypotheses and simplifications introduced in Sec. III. Section V extends the model from stand-alone ORBIT simulations to time-dependent simulations with TRANSP, leveraging the existing *kick model* tools developed in NUBEAM. Section VI summarizes the main results of this work and concludes the paper

II. TARGET SCENARIO: NSTX-U #204083

The reference scenario for this work is a 2-seconds long L-mode NSTX-U [25] discharge with on-axis toroidal field $B_0 = 0.65$ T, current $I_p = 650$ kA and edge safety factor $q_{95} \approx 5 - 6$ [23], see Fig. 1. Neutral beam injection starts at $t = 120$ ms with 1 MW injected at $E_{inj} = 70$ keV throughout the discharge. Both working gas and NB injected neutrals are deuterium. [R1.4]

The equilibrium is recomputed in TRANSP based on the poloidal field diffusion equation, using a fixed boundary constraint computed through the EFIT code [34]. Data from Mirnov coils at the plasma edge indicate repetitive sawtooth crashes starting at $t \approx 420$ ms. The time of sawteeth is used as input in TRANSP to mimic a sudden flattening of the safety factor profile inside the $q = 1$ surface based on a full-reconnection model derived from the Kadomtsev model [6].

The average sawtooth period is $10 - 30$ ms, which is comparable to the sampling time of profile diagnostics measuring electron and ion density and temperature [35][36][37]. Previous work [23] has indicated that changes in the thermal profiles can be as important as fast ion redistribution for the resulting TRANSP results, for instance in terms of computed neutron rate and fast-ion deposition profiles, hence affecting the computed fast-ion distribution. To include the effect of thermal profile flattening caused by sawteeth in the TRANSP simulations for this scenario, the original profile data are resampled through conditional average [23]. The resampling introduces uncertainties in the actual profile evolution, which do not affect the benchmark discussed herein.

III. DESCRIPTION OF THE WORKFLOW

The new model is implemented in the ORBIT code [27]. ORBIT is a Hamiltonian guiding-center particle following code that evolves test particles (or *markers*) in a given equilibrium field. Perturbations can be introduced in the code to explore their effect on particle transport. ORBIT has been extensively used to study fast particle transport induced by a broad range of instabilities, including fishbones [38], Alfvénic modes [39][40], tearing modes [41][42][43] and sawteeth [16][44][23].

ORBIT reads the equilibrium information at a selected time from the EFIT output, or an equivalent output generated from TRANSP simulations. The equilibrium is converted into bicubic splines on a 2D poloidal cross-section in Boozer coordinates, assuming axi-symmetry [45].

Typical ORBIT runs read perturbation data from MHD codes such as NOVA [46]. For the new sawtooth model, an analytic expression can also be used as an alternative to the MHD code output. This makes the model self-contained since it does not require additional inputs, besides the

equilibrium information. The validity of this approach is discussed in Sec. III A for the reference NSTX-U case examined in this work.

Markers covering all possible orbit types (passing, trapped, stagnation, potato) are initialized in two different ways depending on the required output. For stand-alone simulations, markers are sampled from a fast-ion distribution produced by the NUBEAM module of TRANSP, see Sec. III C. When the model is used to generate transport coefficients for NUBEAM, a uniform deposition in fast ion phase space is used instead [33].

During the simulation, the mode amplitude varies as an exponential growth followed by a fast decay, cf. Sec. III B. The duration of the simulated sawtooth cycle, as several other parameters, is set through a *namelist* controlled by the user. The model can run with a maximum mode amplitude specified by the user, or with an automatic algorithm to determine the expected maximum mode amplitude as explained in Sec. III B.

The output of the simulation is a sequence of files with information on the fast-ion distribution during the run. Times at which the files are dumped, as well as the duration of the time window over which data are accumulated, are selected by the user. The output files have the same structure as the original NUBEAM output file used to initialize the marker, see Sec. III C, with updated information on the fast-ion distribution evolution. Alternatively, when a uniform distribution of markers is used, the model produces fast ion transport matrices that can be used as input to the kick model implemented in NUBEAM for time-dependent simulations that include the effects of sawteeth.

A. Mode structure for internal kink

Figure 2a shows a poloidal cross-section of NSTX-U with contours of the poloidal flux, normalized to its value at the last closed flux surface, just before a sawtooth crash. The safety factor profile, shown in Fig. 2b, reaches a minimum $q_0 \approx 0.85 - 0.9$ before the crash. The $q = 1$ surface is located inside the mid-radius near $\Psi_{pol} = 0.4$, so that a relatively large region of the plasma is affected by the instability.

Based on the equilibrium computed by TRANSP and the reconstructed plasma profiles, the NOVA code is used to compute the radial mode structure of the $n = 1$ internal kink. The mode structure is shown in Fig. 2c in terms of its $\alpha_{m,n}(\Psi_{pol})$ coefficients [47], which are related to the magnetic field perturbation components $\delta\mathbf{B}_{m,n}$ and the associated radial displacement $\xi_{m,n}$ through Eqs. 1a-1c.

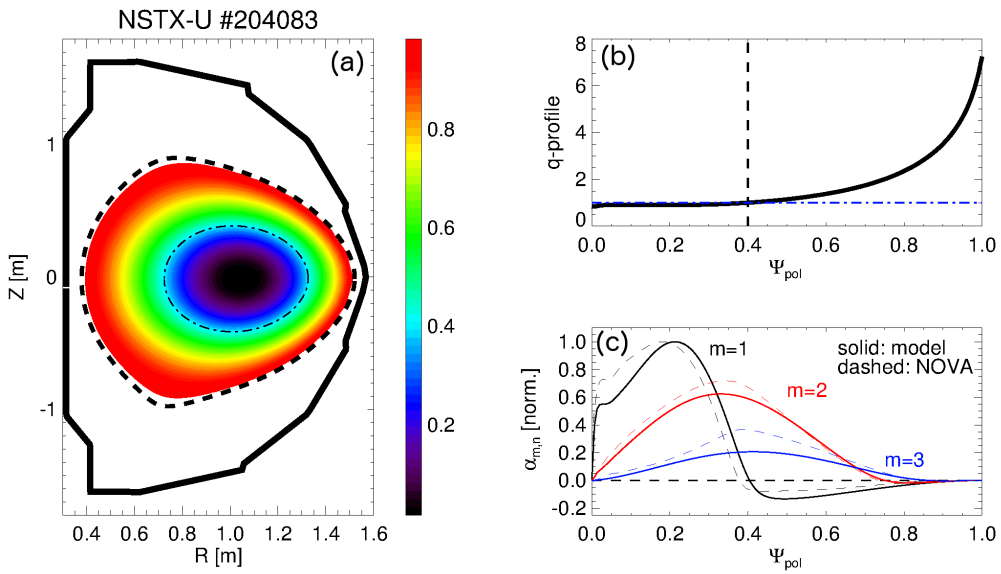

FIG. 2: (a) Contour plot of normalized poloidal flux for NSTX-U #204083 around $t = 720$ ms, just before a sawtooth. Lines in the plot indicate the position of the vessel wall (solid), last closed flux surface (dashed) and $q = 1$ surface (dot-dashed). (b) Safety factor profile as a function of poloidal flux normalized to its edge value, Ψ_{pol}. The vertical dashed line indicates the position of the $q = 1$ surface just before a sawtooth crash. (c) Coefficients $\alpha_{m,n}(\Psi_{pol})$ from the analytic representation in Eqs. 2a-2c (solid) and from NOVA (dashed).

$$\delta \mathbf{B}_{m,n} = \nabla \times \alpha_{m,n} \mathbf{B}, \tag{1a}$$

$$\xi_{m,n}\left(\Psi_{pol}\right) = \alpha_{m,n}\left(\Psi_{pol}\right) \frac{mg + nI}{m/q - n}, \tag{1b}$$

$$\delta B_r = \delta \mathbf{B} \cdot \nabla \psi_p = \sum_{m,n} \frac{mg + nI}{J} \alpha_{m,n}\left(\Psi_{pol}\right) \cos\left(n\zeta - m\theta - \omega t\right). \tag{1c}$$

In Eqs. 1a-1c, n and m are the toroidal and poloidal mode numbers. θ, ζ are the poloidal and toroidal angles in Boozer coordinates. g and I are the current poloidal and toroidal functions [45]. J is the Jacobian in the (ζ, Ψ, θ) Boozer coordinate system. ω is the angular mode frequency and t is time. In the following, a constant $\omega = 2\pi f$ with $f = 10$ kHz is used, which corresponds to the core toroidal rotation frequency in the laboratory frame.

When results from MHD codes are not readily available, especially for extensive scans of the input equilibrium properties (e.g. for sensitivity studies based on the input q-profile), it may be convenient to use analytic expressions for the mode radial structure instead of relying on external

codes. Several approximations for the $n = 1$ internal kink structure have been proposed in previous works, cf. [16][9][48][49][23] and references therein. Most expressions approximate the dominant $n = 1$, $m = 1$ component of the radial displacement as a hat-like function extending from the magnetic axis to the $q = 1$ surface. Constraints from ideal MHD and quasi-neutrality are used in other works [48][45], often based on large-aspect-ratio or cylindrical approximations coupled to ideal MHD and quasi-neutrality conditions. For this work, an analytic expression inspired by Refs. [16][9] and a comparison with eigenmodes from NOVA is proposed for the $\alpha_{m,n}$ coefficients:

$$\alpha_{m,n}(\Psi_{pol}) = \frac{\alpha_0}{m^P} \left(\frac{\Psi_{pol}}{\Psi_{q=m/n}} \right)^m (1 - \Psi_{pol})\ G(\Psi_{pol})\, H_{m,n}(\Psi_{pol}), \tag{2a}$$

$$G(\Psi_{pol}) = \frac{n\,q - m}{g\,q + I}, \tag{2b}$$

$$H_{m,n}(\Psi_{pol}) \propto \tan^{-1}\left[-2\pi \frac{\Psi_{pol} - \Psi_{q=m/n}}{M\kappa(\Psi_{pol})\Psi_{q=m/n}} \right]. \tag{2c}$$

where α_0 is a common scale factor, $\Psi_{q=m/n}$ is the radial location where $q(\Psi_{pol}) = m/n$ and $\kappa(\Psi_{pol})$ is the local elongation of the magnetic surfaces. The function $H_{m,n}(\Psi_{pol})$ is introduced to provide a smooth transition from large to smaller values of $\alpha_{m,n}$ across the $q = m/n$ surface. Its value is renormalized to lie between 1 near the magnetic axis to 0 at the plasma edge. The smoothness of the transition region can be adjusted through the M parameter, which is set to $M = 0.5$ for this work. The second free parameter, P, is used to scale the relative amplitude of harmonics for increasing m's values. Its value here is set to $P = 3$.

With the choice of free parameters $M = 0.5$ and $P = 3$, the expression for $\alpha_{m,n}$ ($m = 1, 2, 3$) from Eqs. 2a-2c shows a satisfactory agreement with the NOVA solutions, see Fig. 2c. (Although the agreement deteriorates as m increases, higher poloidal harmonics become less and less important from the point of view of fast ion transport.) More scenarios need to be analyzed for a more complete assessment of the generality of Eqs. 2a-2c for a broader set of sawtoothing scenarios, including on other devices.

B. Time evolution and peak value of mode amplitude

The general features of mode amplitude evolution during a sawtooth cycle are well known from experiments [6][4]. In essence, as the safety factor on axis decreases below $q_0 = 1$ the mode undergoes a fast growth on time scales of the order of milliseconds or less, then suddenly crashes in

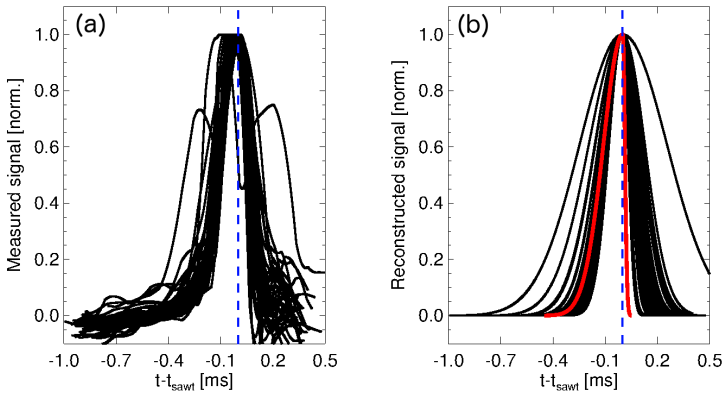

FIG. 3: (a) Ensemble experimental signals from Mirnov coils during sawtooth crashes for NSTX-U discharge #204083. Traces are normalized to their peak value and shifted in time with respect to the estimated time of peak sawtooth amplitude, t_{sawt} (vertical dashed line in both panels). (b) Fits of data from panel (a) based on Eq. 3 (black curves) and their pre-crash average, followed by a fast decay post-crash (red line).

what is a full reconnection event following the original Kadomtsev model [6], or partial reconnection based on the Porcelli model [50]. So-called *pre-cursor* and *post-cursor* instabilities are sometimes observed in experiments before and after sawtooth crashes. Their role is neglected in this work, although they may play a significant role in the overall understanding of the sawtooth stability and dynamic. For simplicity, it is assumed here that pre-cursors and post-cursors appearing on time scales much longer than the sawtooth crash duration - and, arguably, with lower peak amplitude - do not alter significantly the estimates of fast ion transport. However, more work is needed to confirm (or confute) that assumption.

The amplitude evolution in ORBIT, $A_{sw}(t)$, is modeled through Eq. 3:

$$A_{sw}(t) = A_0 \times \begin{cases} e^{-\left[\frac{(t-t_{sawt})^2}{\Delta t_1^2}\right]}, & t \leq t_{sawt} \\ e^{-\left[\frac{(t-t_{sawt})^2}{\Delta t_2^2}\right]}, & t > t_{sawt} \end{cases} \tag{3}$$

where $\Delta t_1 = 0.35\, f_{sw}\, T_{sim}$ and $\Delta t_2 = 0.35\,(1 - f_{sw})\, T_{sim}$, with T_{sim} the duration of the simulation (corresponding to the duration of the simulated sawtooth cycle) and f_{sw} a free parameter set by the user. t_{sawt} is the time of peak sawtooth amplitude, and the coefficient 0.35 is used to enforce a negligible amplitude $A_{sw} \lesssim 5 \times 10^{-3}$ at the beginning and at the end of the cycle. The purpose of the f_{sw} parameter is to skew the amplitude evolution to a slower growth before $t = t_{sawt}$, followed by a faster decay after the crash. In this work, $f_{sw} = 0.8 - 0.9$ with negligible dependence of the final results on its exact value within that range. The scaling coefficient A_0 sets the peak mode

amplitude achieved during the simulation, as discussed below.

Adjustable parameters in Eq. 3 can be estimated directly from experimental data. Figure 3a shows the envelope of signals from a Mirnov coil filtered in the $5 - 20$ kHz frequency range. Data are centered around the estimated sawtooth crash times, t_{sawt}. Figure 3b shows the result of a fit of the experimental data using Eq. 3 to determine Δt_1. The fit assumes a zero baseline for the mode evolution, consistent with neglecting precursor activity. The value of Δt_2 is determined by setting $f_{sw} = 0.9$, i.e. assuming a faster decay than observed in the experimental data. This choice is qualitatively justified by (i) neglecting the contribution of post-cursors to the magnetics' signal, and (ii) mimic a fast crash that happens on time scales comparable to the toroidal transit time of fast ions, which is of order of 10 μs for fast ion energies ≈ 70 keV. On the latter point, it is important to note that equilibrium quantities such as the q-profile are kept constant during the ORBIT simulation, so detailed physics of the crash and reconnection events are missing. This is likely to result in underestimating the fast ion transport, especially for the lower energy particles below the critical energy.

The next step in the model is to provide an estimate for the peak mode amplitude during the crash, A_0 in Eq. 3. The obvious solution is to use experimental data to infer A_0. Unfortunately, such information is not readily available in many cases. The approach adopted for the new sawtooth model to estimate A_0 is to rely on experimental evidence that thermal plasma profiles are flattened inside the $q = 1$ surface, at least for the largest amplitude events. In practice, this is equivalent to adopt a "full reconnection" approach as in the Kadomtsev model, thus providing an upper estimate for the peak mode amplitude and a worst-case scenario for the resulting fast ion transport.

The new implementation in ORBIT includes a module to estimate A_0 based on the assumption that thermal particles are fully redistributed from the magnetic axis up to the $q = 1$ surface. The algorithm deposits N_p pairs of markers with energy 0.1 keV, representative of thermal particles, near the axis and near the $q = 1$ surface. Each pair is initialized at different toroidal angles, so that markers have different initial phases with respect to the perturbation. Due to their low energy, thermal particles can be assumed to follow the magnetic field lines. Their orbit displacement in Ψ_{pol} is then indicative of the underlying perturbation of the magnetic field. Particles are evolved over a sawtooth cycle with amplitude $A_{sw}(t)$ given by Eq. 3, and the maximum excursion in Ψ_{pol} is recorded. The peak amplitude A_0 is adjusted iteratively until either a particle born near the axis reaches the $q = 1$ surface, or a particle deposited near $q = 1$ reaches the magnetic axis. Once that happens, it is assumed that the perturbation amplitude A_0 is such that magnetic field lines between the axis and the $q = 1$ surface can reconnect.

Figure 4 shows an example of an amplitude A_0 scan to determine the peak sawtooth amplitude. At negligible perturbation amplitude $A_0 = 10^{-6}$ the thermal markers follow the magnetic field lines. As the amplitude is increased to $A_0 = 2 \times 10^{-3}$, perturbations in the markers' orbit start to appear but they are not strong enough to suggest that "recombination" may occur. As the amplitude is further increased to $A_0 = 10^{-2}$, markers deposited near the $q = 1$ are displaced inward and reach the unperturbed magnetic axis. A further increase in the mode amplitude A_0 leads to stochastic orbits for the thermal markers, extending further out in radius well beyond the $q = 1$ surface. According to the algorithm implemented in ORBIT, $A_0 \approx 10^{-2}$ provides the solution for the peak mode amplitude for this specific scenario. It is expected that values can differ considerably based on the initial q-profile. For instance, frequent sawteeth tend to result in a $q = 1$ surface located closer to the magnetic axis than "monster" sawteeth, thus frequent sawteeth will result in a smaller amplitude. This expected behavior will be tested on other devices in future publications [51][52].

A more quantitative assessment of the effect of the mode on thermal plasma profiles is shown in Fig. 5 for the amplitude A_0 identified from ORBIT. Assume that N markers are initialized in ORBIT uniformly along Ψ_{pol}. The initial position and associated volume, $\Psi^0_{pol,k}$ and $\Omega^0_k = \Omega(\Psi^0_{pol,k})$, are recorded ($k = 1 \ldots N$) along with the corresponding density and temperature, $n^0_{e,k}$ and $T^0_{e,k}$. Profiles are taken from TRANSP just before a sawtooth event. During the simulation, markers move to different locations $\Psi^i_{pol,k}$, and the associated volume $\Omega^i_k = \Omega(\Psi^i_{pol,k})$ is recorded. The "post-sawtooth" density and temperature are reconstructed on the same Ψ_{pol} grid used by TRANSP based on recorded values from the last 20% of the simulated sawtooth cycle, which is when the instability is mostly active in ORBIT. Density and temperature from the redistributed markers (cf. Fig. 4c) are averaged on the TRANSP Ψ_{pol} grid, with each marker contributing by a factor $n^0_{e,k}\Omega^0_k/N_{samp}\Omega^i_k$ for density and $T^0_{e,k}n^0_{e,k}\Omega^0_k/N_{samp}\Omega^i_k$ for temperature to account for regions with a different volume. N_{samp} is the number of markers at each TRANSP Ψ_{pol} grid point. An uncertainty for the reconstructed T_e and n_e following the sawtooth cycle is also assigned as the reconstructed density and temperature divided by the square root of the number of markers falling in each bin. As can be seen from Fig. 5, the amplitude inferred from ORBIT results in a flattening of both reconstructed T_e and n_e inside the $q = 1$ surface that is in good agreement with the raw and re-processed experimental profiles. This comparison provides evidence that the peak amplitude estimated through ORBIT is in reasonable agreement with the experimental mode amplitude, given all the assumptions and simplifications adopted in the ORBIT analysis. [R1.5]

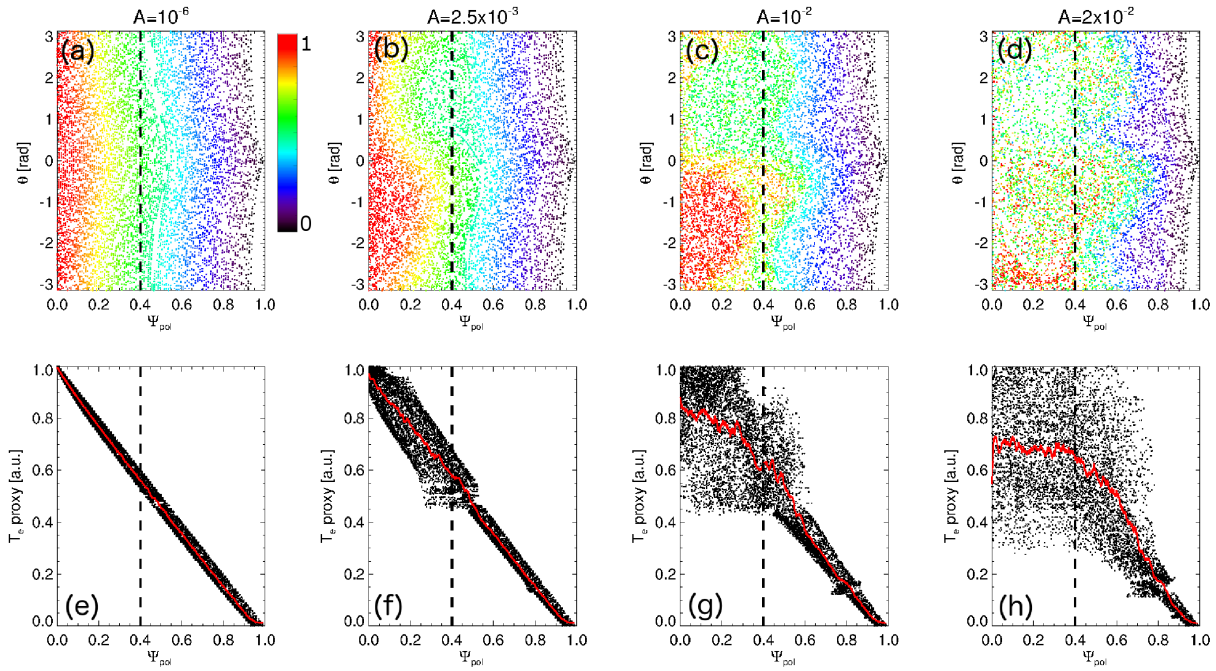

FIG. 4: Example of amplitude scan in ORBIT to infer the peak kink amplitude, with $10^{-6} \leq A_0 \leq 2\times10^{-2}$. Markers are assigned a value $w = 1 - \Psi_{pol,0}$, where $\Psi_{pol,0}$ is their radial position at the beginning of the simulation. The color is indicative of the initial marker position, from red (magnetic axis) to black (plasma edge) as indicated by the color bar in panel (a). Markers are selected from a time window of ± 50 μs centered at $t = t_{sawt}$. (a-d) Show the markers as a function of poloidal flux and poloidal angle. (e-h) Projection of the markers from (a-d) onto Ψ_{pol} (black dots) and average profile of the marker (red lines). The latter can be interpreted as a rough proxy for the electron profiles, thus providing an indication of the core flattening caused by the sawtooth.

C. Sampling of the initial markers from NUBEAM

When used as a stand-alone analysis tool, initial markers for a selected fast ion species (e.g. deuterium, tritium or fusion products) are initialized based on an unperturbed fast-ion distribution, $F(E, p, R, Z)$, produced by the NUBEAM module of TRANSP about 1 ms before the sawtooth event of interest. Here E is energy, $p = v_{par}/v$ is the pitch (ratio of parallel to total velocity), and (R, Z) are the radial and vertical coordinates in a poloidal cross-section. NUBEAM divides the cross-section inside the last closed flux surfaces in a certain number of Monte Carlo (MC) zones, see Fig. 6a. An increasing number of MC zones is used as their radial coordinate (uniform in *toroidal* flux) increases from the axis to the edge. For 10 radial zones in the 1D output profiles, 220 MC zones are used to cover the cross-section.

The 4D distribution $F(E, p, R, Z)$ is sampled in ORBIT using a Monte Carlo approach. For each

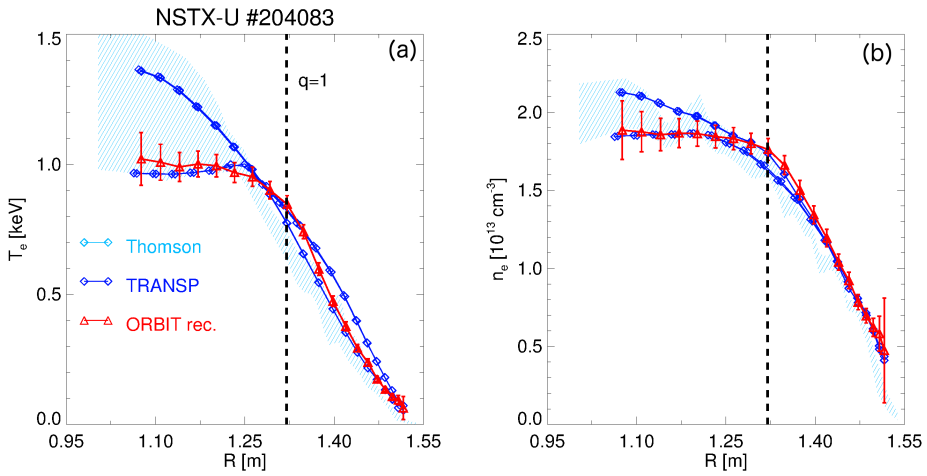

FIG. 5: Comparison of the expected electron temperature and density flattening for peak mode amplitude A_0 inferred from ORBIT with profiles from the experiment (Thomson scattering) and TRANSP (conditionally averaged reconstruction). (a) T_e profiles from TRANSP (blue) and reconstructed based on kinetic Poincaré runs from ORBIT (red). The shaded area in light blue is obtained as the envelop of measured profiles from Thomson scattering over ≈ 110 ms, which include profiles measured at different phases of sawtooth cyles. (b) Same as in (a) for the electron density, n_e. The vertical dashed line indicates the radial location of the $q = 1$ surface before a sawtooth.

marker, the distribution integrated over p, R, Z is first used to extract a random ρ_{tor} (equivalently, Ψ_{pol}). The extraction can be biased through a user-selected weight factor w_a based on $w_\rho = 1-\rho_{tor}^{w_a}$. Values $w_a < 1$ lead to more particles with smaller weight to be extracted near the core, which helps to keep good statistics for centrally-peaked fast-ion profiles. Once ρ_{tor} (eq. Ψ_{pol}) is selected, the algorithm selects a random (R, Z) MC zone at that ρ_{tor}, thus identifying the poloidal angle θ. Finally, random energy and pitch are extracted from $F(E, p, R, Z)$ for the given (R, Z) and a random toroidal angle ζ is assigned to the marker.

Similar to what is implemented in NUBEAM, the fast-ion distribution in ORBIT (from which the density is computed either as a function of MC zone or of ρ_{tor}) is averaged at given times during the simulation over a time window selected by the user. An example of the results from the sampling procedure described above is shown in Figs. 6b-c in terms of fast-ion density profile vs MC zone and ρ_{tor} from the original NUBEAM file and from ORBIT. For this example (and for the rest of the paper), 50k markers are used in ORBIT with $w_a = 0.5$ and 64k particles in NUBEAM. The averaging time is ± 100 μs in ORBIT and 1 ms in NUBEAM. Overall, the agreement in radial fast-ion density is within a few percent, with the largest discrepancy near the magnetic axis.

More details are given in Fig. 7 in terms of fast-ion distribution $F(E, p)$ at two radial locations,

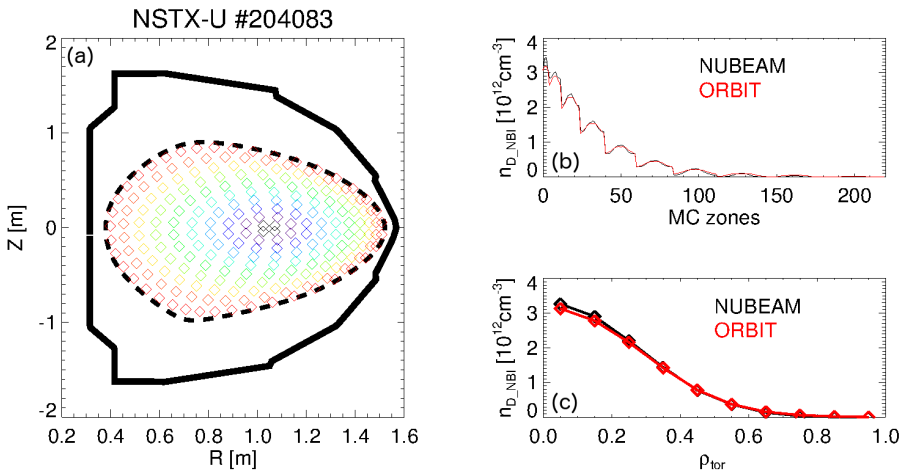

FIG. 6: (a) Cross-section of NSTX-U showing the NUBEAM MC zones (diamonds) color-coded based on their corresponding ρ_{tor} position. The dashed line indicates the last closed flux surface, and the thick solid line is the contour of the NSTX-U wall. (b) Fast-ion density from NUBEAM (black) and ORBIT (red) as a function of MC zones used in NUBEAM. (c) 1D fast-ion density profile from NUBEAM and ORBIT as a function of toroidal flux, ρ_{tor}.

near the axis and close to mid-radius. From the figures, the fast-ion distribution details are well recovered by the ORBIT sampling. Numerical noise is mostly attributed to the relatively low number of MC markers used in the original NUBEAM/TRANSP run. However, even when only $50k$ markers are used in ORBIT, the numerical noise in the fast-ion distribution does not affect integrals of the distribution such as radial density of fast ions, as shown below in Fig. 8a. (For scenarios that require a broader energy range, e.g. when fusion products or RF tails are present, it is expected that the number of MC markers needs to be increased substantially to provide a correct sampling of the original fast-ion distribution from NUBEAM). [R1.1]

IV. EVOLUTION OF FAST-ION DENSITY AND DISTRIBUTION FUNCTION

Bringing together the different elements discussed in Sec. III, this Section presents initial results for fast ion redistribution by sawteeth for the NSTX-U scenario introduced in Sec. II. The workflow is applied to compute the fast-ion distribution modification by a sawtooth with duration $T_{sim} = 0.6$ ms, as derived from the experiment. The normalized peak mode amplitude is $A_0 = 10^{-2}$. 50k markers are used for the ORBIT simulation. The distribution function, from which the radial fast-ion density profile is computed, is sampled in ORBIT at $t - t_{sawt} = -.48, -0.28, -0.08, 0.12$ ms with an averaging time window of ± 50 μs.

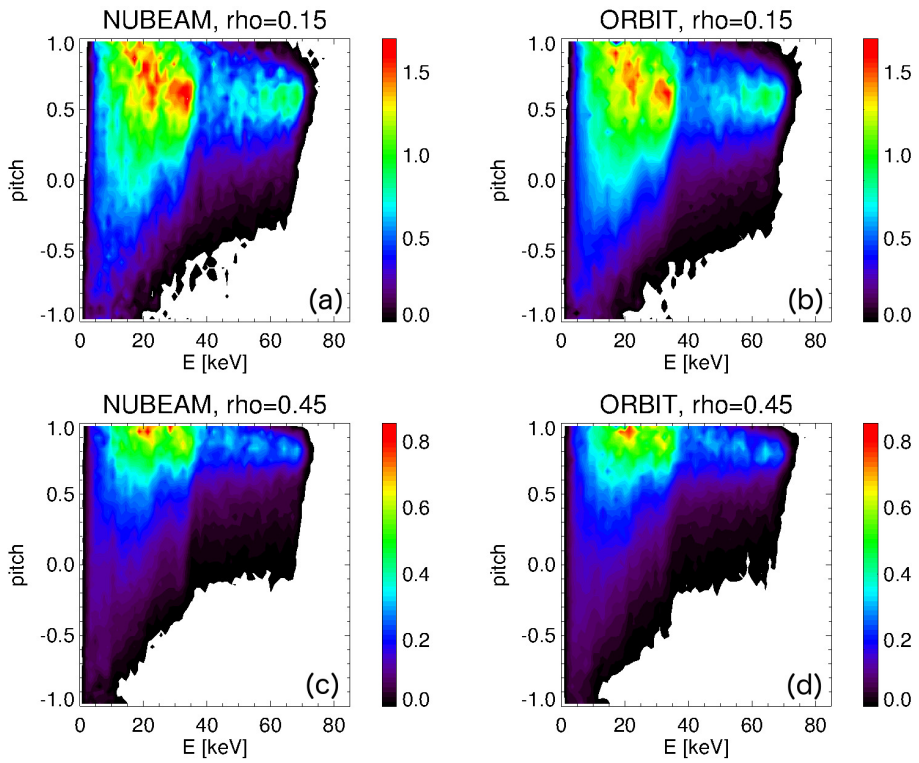

FIG. 7: Comparison of the original fast-ion distributions $F(E,p)$ from NUBEAM at two radial locations (a,c) with the same distributions as sampled by ORBIT (b,d). Color bar units are $10^8/cm^3/eV/4\pi$.

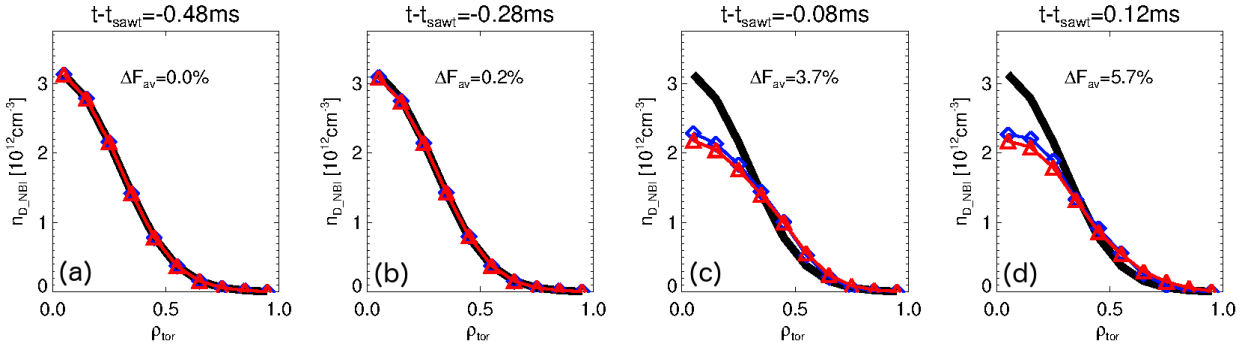

FIG. 8: Time sequence of fast-ion density during a simulated sawtooth cycle for NSTX-U #204083. The pre-crash density is shown as black line as a reference. Blue and red line show the ORBIT results using the radial mode structure from NOVA and from Eqs. 2a-2c, respectively. Values ΔF_{av} indicate the relative discrepancy, averaged over ρ_{tor}, between runs using mode structure from ORBIT or NOVA.

The simulated evolution of the fast ion radial density profile is shown in Fig. 8. Results from ORBIT using the radial mode structure from NOVA and from the analytic representation from Eqs. 2a-2c are in good agreement, with average relative discrepancy $\leq 6\%$ near the peak mode amplitude. [R1.3]

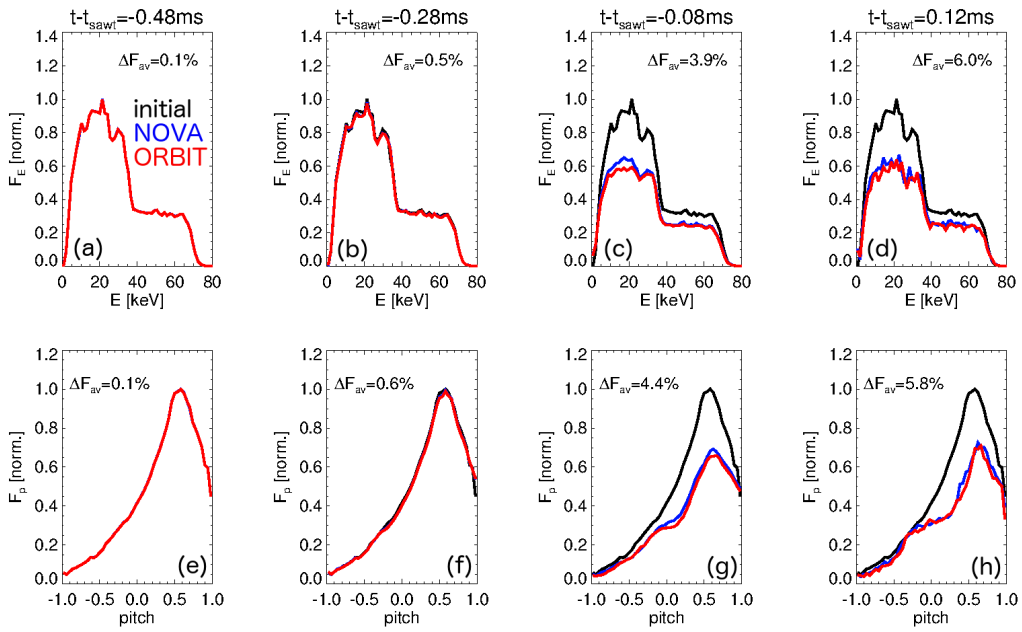

FIG. 9: Time sequence of the fast-ion distribution at $\rho_{tor} = 0.05$ during a simulated sawtooth cycle for NSTX-U #204083. The pre-crash distribution is shown as a black line for reference. Blue and red lines show the ORBIT results using the radial mode structure from NOVA and from Eqs. 1a-1c, respectively. (a-d) fast-ion distribution integrated over pitch. ΔF_{av} indicates the relative discrepancy between runs using mode structure from ORBIT or NOVA. (e-h) fast-ion distribution integrated over energy. All distributions are normalized by the same scale factor.

The fast-ion density is the result of integrals over several fast ion parameters - namely energy, pitch and MC zones. As such, it may not be a clear indicator of potential differences in results caused by different assumptions used in the model, for examples on the radial perturbation profiles (NOVA vs analytic). As implemented in ORBIT, the new workflow provides the required additional details on the evolution of the fast-ion distribution as a function of energy and pitch during a simulated crash. Figures 9 and 10 show results for the fast-ion distribution $F(E, p)$ changes near the magnetic axis and near the $q = 1$ surface. Overall, the model shows an agreement within 6% between the results from ORBIT runs using the NOVA radial mode structure and the analytic formula from Eqs. 2a-2c . [R1.3]

In addition to providing a benchmark for the validity of Eqs. 2a-2c, the results shown in Figs. 8, 9 and 10 capture the main features of fast ion redistribution that can be studied through this framework. Notably, the reduction in fast-ion density is already apparent before the nominal crash time (Fig. 8c). This is because of the contribution of *resonant* fast ion transport to the overall transport channels [16][15]. The sudden drop in mode amplitude after $t = t_{sawt}$, which mimics a fast [R1.3]

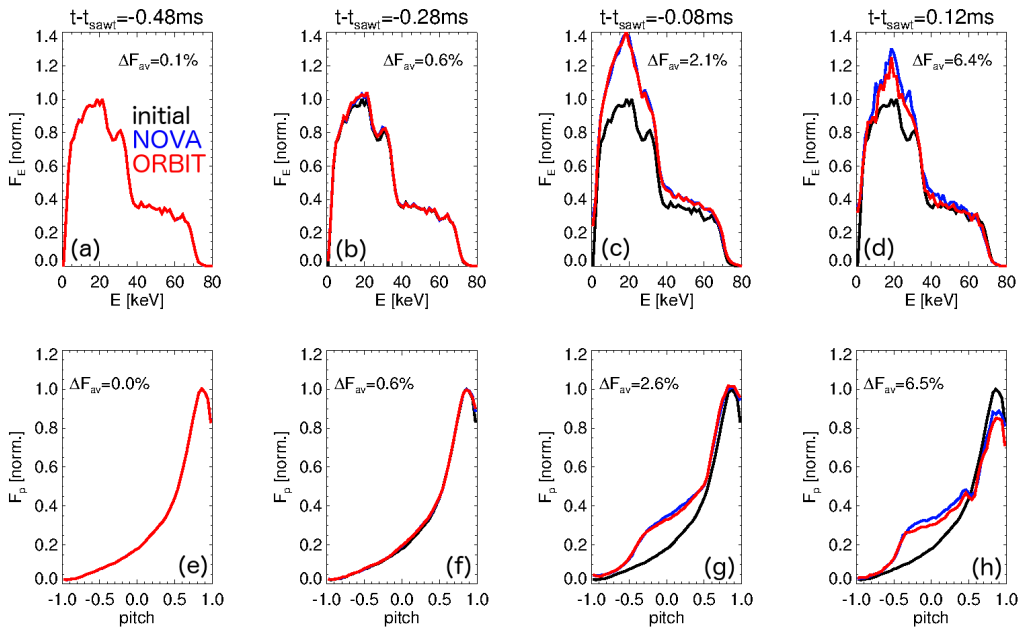

FIG. 10: Same as in Fig. 9 for $\rho_{tor} = 0.45$, near the $q = 1$ surface.

change in magnetic topology, seems to provide a negligible contribution to the overall redistribution of fast ions for this case. For this scenario, estimates of the critical energy for redistribution of fast ions is ≈ 30 keV for trapped particles and $\gg E_{inj}$ for passing particles, where $E_{inj} = 72$ keV is the NB injection energy [23]. Since most trapped particles have energies $\lesssim 40$ keV (cf. Fig. 7), virtually all particles inside the $q = 1$ surface can be redistributed by non-resonant processes. The redistribution of particles with different orbit type is confirmed by Figs. 9-10, which show depletion of the distribution near the core over a very broad range of energy and pitch, and redistribution of particles at radii around $q = 1$. Effects are more pronounced for trapped particles, likely due to their large orbit width of several centimeters.

Additional information (not shown in this work) can be gathered by analyzing EP transport in terms of phase space, including breaking down the EP population by orbit type. Such analysis is convenient to identify relaxation of the EP fast-ion distribution, which is related to the stability of other instabilities that can be triggered or suppressed by the crash [53].

V. TRANSFER OF THE FAST ION TRANSPORT COEFFICIENTS TO TRANSP

A. The MHD *kick model* in NUBEAM

Fast ions are modeled in TRANSP [13][28] by the Monte Carlo module NUBEAM [29][30], which includes collisional scattering, slowing-down, and atomic physics processes such as charge-exchange and neutralization reactions. In addition, NUBEAM includes a physics-based reduced model, called *kick model* [32][33] to mimic the effects of instabilities on fast ion transport. The *kick model* relies on particle-following codes such as ORBIT to distill information on EP transport that can then be used in TRANSP/NUBEAM to evolve the fast-ion distribution including the effect of instabilities.

The main input for a TRANSP/kick model simulation is a set of transport probability matrices that condense the effects of instabilities on energetic particle. Matrices are defined over the constant of motion variables E, P_ζ and μ, which represent the fast-ion energy, canonical toroidal angular momentum and magnetic moment [40][45]. For each (E, P_ζ, μ) region in phase space, the matrix contains a probability $p(\Delta E, \Delta P_\zeta)$ of correlated fast-ion energy and P_ζ changes (or *kicks*) caused by the instabilities. Each probability matrix can represent the effects of a single perturbation, or a set of perturbations with similar temporal evolution.

The transport matrix is computed via particle following codes such as ORBIT [27]. For Alfvénic modes that can feature a large number of poloidal harmonics and a complex radial mode structure, mode structures are computed through MHD codes such as NOVA/NOVA-K [46][54][55]. As discussed in Sec. III A, low-frequency modes such as kinks, tearing modes and fishbones are usually characterized by simpler mode structures that can be approximated by analytical expressions. To compute a kick probability matrix in ORBIT, the EP phase space is divided into discrete bins to group particles with similar phase space coordinates. Typical numbers of bins for the E, P_ζ and μ are $n_E \sim 10 - 15$, $n_{P_\zeta} \sim 30 - 40$ and $n_\mu \sim 14 - 20$. The evolution of (E, P_ζ, μ) of each particle is recorded in ORBIT during the simulation at sampling intervals δt_{samp}. For Alfvénic modes, the value of δt_{samp} is chosen to be larger than the period of the instability to filter out fast oscillations and mostly retain changes over the longer time scales associated with particles being trapped in a resonance. Eventually, thousands of $\Delta E, \Delta P_\zeta$ samples are accumulated for each phase space bin. These samples are used to compute the two-dimensional histogram $p(\Delta E, \Delta P_\zeta)$ on a finite ΔE, ΔP_ζ grid. Once the procedure is extended to the whole phase space, the result is a five-dimensional transport matrix $p(\Delta E, \Delta P_\zeta | E, P_\zeta, \mu)$.

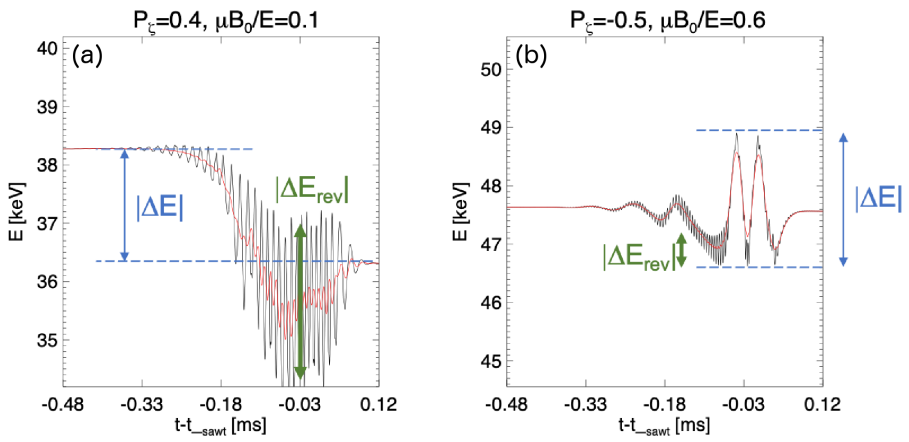

FIG. 11: Example of reversible vs irreversible changes in energy. The faster time scales are associated with the toroidal transit time of the particles, which results in oscillations around the slower energy change caused by resonant interaction with the low frequency mode. (a) Co-passing particle near the magnetic axis. (b) Co-passing particle outside the $q = 1$ surface. Black lines are the raw energy vs time, whereas the red lines are a low-pass filtered version used to compute the energy kicks. The amplitude of the perturbation is the same as shown in Fig. 3b.

Kick amplitudes during a TRANSP/kick run are scaled as a function of time according to a waveform $A_{mode}(t)$ that is provided as input to TRANSP. For interpretive runs, mode amplitudes are inferred from available experimental data, e.g. from Mirnov coils or internal measurements from reflectometers, interferometers or electron-cyclotron emission (ECE) systems. For TRANSP/kick simulations with sawteeth, $A_{mode}(t)$ is constructed by replicating the waveform in Fig. 3b at each sawtooth event.

More details on the kick model algorithm in ORBIT are given in the Appendix of Ref. [33].

B. Computation of kick probabilities for large mode amplitude and low frequency

The extension of the kick model to sawteeth requires special considerations compared to previous work on Alfvénic modes, mostly due to the lower frequency and larger amplitude of internal kinks with $\delta B/B_0 \sim 10^{-2}$.

A first issue is the long wave period compared to characteristic frequencies of the fast particle motion. For a kink frequency $\approx$ 10 kHz and fast-ion energy $\approx$ 80 keV typical of NSTX-U, the transit time is much shorter than the wave period. This results in fast changes in most fast ion variables that are not caused by resonant interaction and do not cause net changes in E, P_ζ. An example is shown in Fig. 11a for a co-passing particle that shows reversible oscillations in energy of

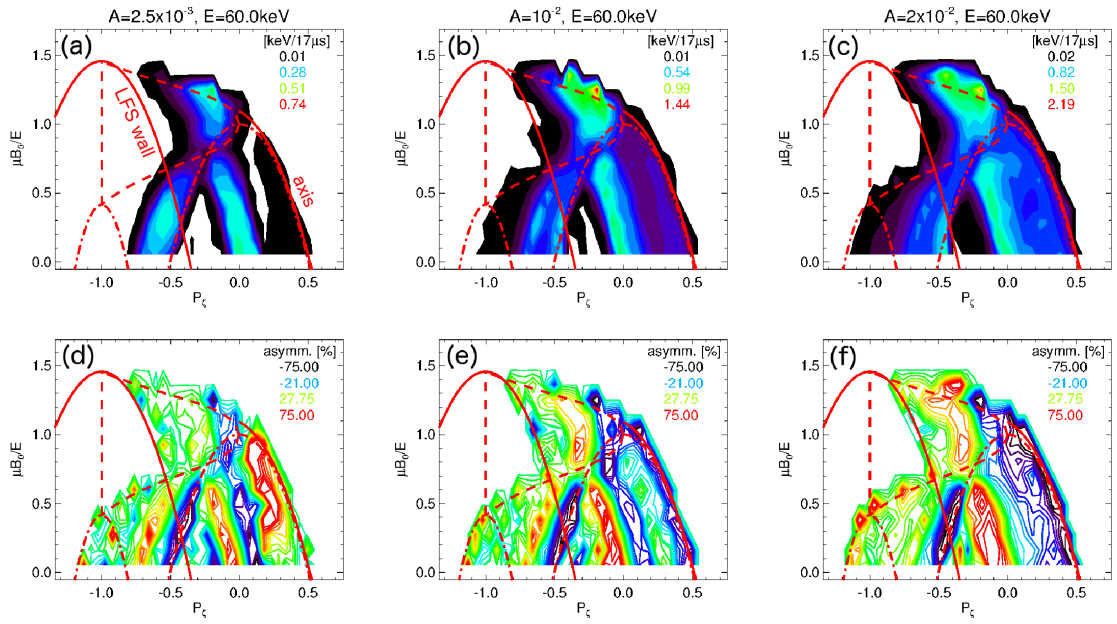

FIG. 12: (a-c) Root-mean-square energy change for 60 keV fast ions as a function of phase space coordinates for different values of mode amplitude. (d-f) Asymmetry in energy kicks. Positive (negative) values mean kicks are skewed toward positive (negative) energy kicks, which translate in positive (negative) changes in P_ζ. Note the changes in kick features, especially near the magnetic axis (dashed curve for $P_\zeta > 0$, as indicated in panel (a)), as the amplitude is increased from $A = 2.5 \times 10^{-3}$ up to $A = 2 \times 10^{-2}$, which requires corrections in the kick values used to build the overall kick probability matrix for a time-dependent $A_{mode}(t)$ in NUBEAM.

± 1 keV, which is comparable to the net variation $|\Delta E| \approx 2$ keV caused by the kink. The amplitude of the reversible changes in E and P_ζ depends on the phase space coordinates of the particle, as shown by the example in Fig. 11b. This particle is initially located outside the $q = 1$ surface and has smaller pitch (larger orbit width). The reversible contribution is reduced, while the resonant changes in energy are comparable to the previous example. To eliminate the reversible kicks from the probability matrix, the sampled E and P_ζ traces are low-pass filtered in ORBIT before kicks are computed, as shown by the red lines in Fig. 11. The low-pass frequency is a multiple of the kink frequency, in order to filter out the faster time scales while preserving non-reversible changes caused by the mode.

A second issue is caused by the rapid change in time of the mode amplitude, see Fig. 3, which can be shorter than the typical time step used in NUBEAM ($1 - 10$ ms or longer). To compute the kick probability for Alfvénic modes, the mode amplitude is kept constant during the ORBIT simulation at a level that corresponds to typical amplitudes at mode saturation. That approach

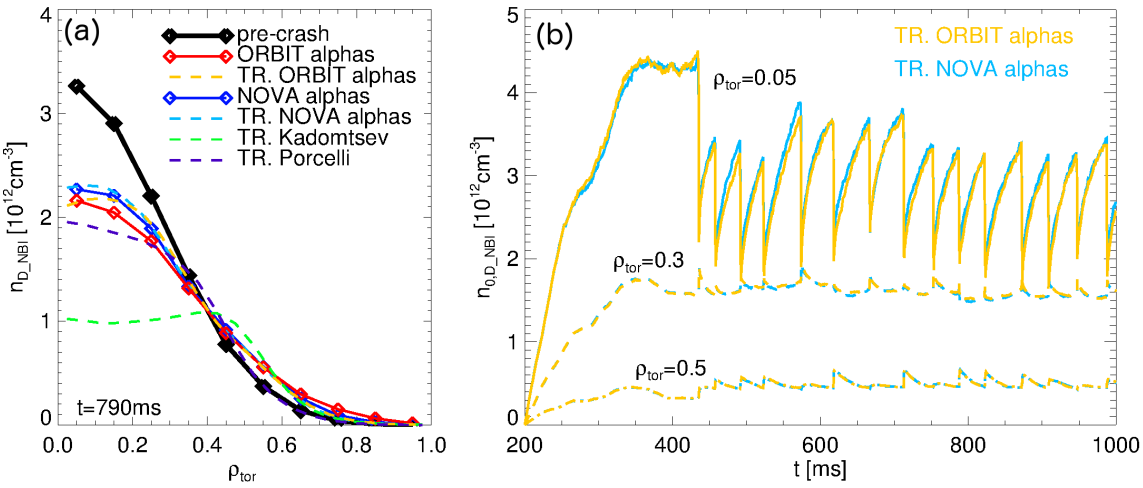

FIG. 13: (a) Fast-ion density profiles from after a sawtooth crash from ORBIT (solid) and TRANSP (dashed). Results obtained using the radial displacement from NOVA are shown in red and light red. Results obtained using the displacement from Eqs. 2a-2c are shown in blue and light blue. The TRANSP profile before the sawtooth event is also shown for reference (thick black line). The redistributed fast-ion density obtained using the Kadomtsev and Porcelli models in TRANSP are shown in green and purple for comparison. (b) Fast-ion density vs time from TRANSP at three radial locations. Light blue curves are based on the NOVA displacement, while yellow curves are based on Eqs. 2a-2c. Results from the Kadomtsev model (not shown) would results in a 2× reduction of the core fast-ion density.

is invalid for sawteeth. As the amplitude evolves, so do the main features that enter into the kick probability matrix, as shown in Fig. 12. Therefore, the amplitude evolution needs to be taken into account, so that the matrix is representative of the entire sawtooth cycle.

In general, the amplitude of resonant kicks scale as $\Delta E(A_{mode}) \propto \sqrt{A_{mode}(t)}$. To build a kick probability that is statistically representative of the entire sawtooth cycle, kicks are stored with their normalized value $\Delta E_k/\sqrt{A_{mode}(t)}$. (Similarly for P_ζ kicks). When combined with the input $A_{mode}(t)$ in NUBEAM, this provides the correct scaling during a macroscopic NUBEAM time step, assuming that kicks are frequent enough to satisfy the Monte Carlo approach on which the kick model is based [32][33].

C. Initial TRANSP/ORBIT comparison

This section presents an initial comparison between the fast ion redistribution computed through ORBIT, following the workflow discussed in the previous sections, and TRANSP results obtained from the kick model based on ORBIT inputs.

Figure 13 compares the post-crash fast-ion density profiles from ORBIT and from TRANSP. Similarly to what has been discussed in Sec. IV, two cases are compared, namely using the radial displacement from NOVA or from the analytic expression in Eqs. 2a-2c The agreement between the time-slice analysis from ORBIT and the full time-dependent TRANSP simulation is remarkable, with differences of a few percent in the post-crash profiles for both cases. Similar small differences are observed during the entire TRANSP simulation (Fig. 13b), with the largest discrepancies recorded near the magnetic axis.

The TRANSP results based on the full-reconnection Kadomtsev model for fast ions [6] are also shown in Fig. 13a. The model assumes full redistribution of *all* fast ions inside the $q = 1$ surface, independent of their energy and pitch. As can be seen from the figure, the Kadomtsev model results in a substantial depletion of fast ions from the core, more than a factor of two from what ORBIT and the TRANSP+kick model simulations predict. The Porcelli model [7] is also implemented in TRANSP. In its simplest implementation, the model assumes reconnection from the $q = 1$ surface up to the magnetic axis (island width fraction = 1). As shown in Fig. 13a, the post-crash fast-ion density based on the Porcelli model is much closer to results obtained from ORBIT than using the Kadomtsev model. [R1.2]

A more detailed comparison of the post-sawtooth distribution functions from ORBIT and TRANSP reveals larger differences than for the fast-ion density profile, see Fig. 14. As shown before in Figs. 9-10, the agreement between runs using either an analytic or NOVA representation for the radial coefficients $\alpha_{m,n}(\Psi_{pol})$ remains within a few percent in both ORBIT and TRANSP/NUBEAM. Qualitative agreement is maintained between the two codes for distributions integrated over pitch or energy at different radii. However, quantitative differences appear between the distributions computed by ORBIT and by TRANSP/NUBEAM. In particular, the distribution from ORBIT shows a *plateau* in pitch near the region populated by trapped particles, $|p| \lesssim 0.3$. The NUBEAM distribution is smoother in pitch. A second difference is the larger fraction of co-passing particles (pitch $p \gtrsim 0.5 - 0.7$) in ORBIT with respect to NUBEAM, especially at larger radii $\rho_{tor} = 0.45$. At present, several possibilities have been considered to explain the differences and further improve the accurate transfer of the kick probability matrices from ORBIT to TRANSP/NUBEAM: [R1.4]

1. Finite Larmor radius (FLR) corrections to EP transport have been excluded as a likely cause for the disagreement. ORBIT simulations that mimic FLR effects by averaging the perturbation over six spatial points around the instantaneous guiding center position show

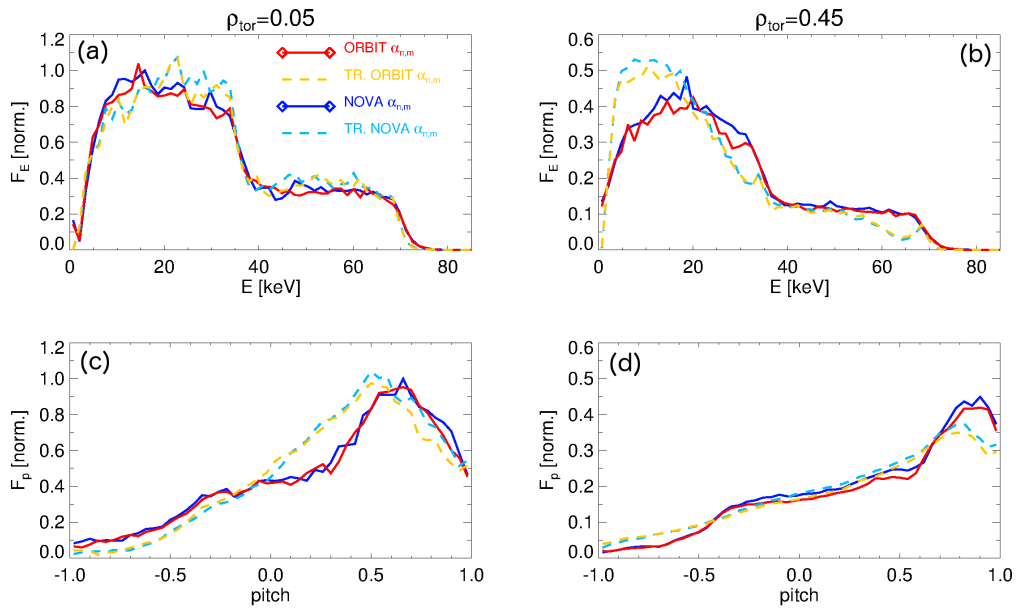

FIG. 14: Comparison of fast-ion distributions after a sawtooth crash from ORBIT vs NUBEAM at $\rho_{tor} = 0.05$ (left column) and $\rho_{tor} = 0.45$ (right column). Blue and red solid lines show the ORBIT results using the radial mode structure from NOVA and from Eqs. 2a-2c, respectively. Dashed lines show results from NUBEAM using analytic $\alpha_{n,m}$ coefficients (light red) and $\alpha_{n,m}$ from NOVA (light blue). (a-b) fast-ion distribution integrated over pitch. (c-d) fast-ion distribution integrated over energy. All distributions are normalized by the same scale factor.

no substantial difference with respect to the standard runs. Transport is slightly reduced for co-passing particles, but remains unchanged for trapped particles characterized by orbit withs similar to - or larger than - a particle's Larmor radius.

2. The NUBEAM distribution is sampled after the crash, thus with a different equilibrium with $q \approx 1$ inside the original $q = 1$ surface. This may lead to changes in orbit topology for particles near the trapped/passing boundary. However, re-processing the ORBIT distribution with the post-crash equilibrium from TRANSP shows similar discrepancies, suggesting that the number of particles that change orbit type because of changes in the underlying equilibrium is small in this case.

3. ORBIT results are low-pass filtered to produce the kick probability matrix, cf. Sec. V B. The effect of reversible changes in the fast ion variables, however, can still appear when sampling the distribution in ORBIT. Fluctuations in Ψ_{pol} (hence in pitch, due to changes of the local magnetic field) may explain the plateau observed e.g. in Fig. 14c for trapped particles. However, as for item #1, re-processing the post-sawtooth distribution from ORBIT with a

zero-amplitude perturbation gives a very similar distribution. It seems thus unlikely that the reversible kicks in ORBIT are responsible for the difference.

4. NUBEAM and ORBIT use different algorithms to sample the fast-ion distribution. However, the discrepancy for trapped particles seems too large to be explained even considering the different implementations. In fact, the pre-crash distributions are in very good agreement. This explanation also seems unlikely.

5. ORBIT simulations do not include sources and sinks, which are include in NUBEAM. Although sawteeth happen on short time scales, comparable or shorter than the NUBEAM time step, sources and sinks may still play a role. Hints for this are the larger discrepancies observed in Fig. 14 at energies close to the injection energy and 1/2, 1/3 NB energy components. This possibility cannot be completely ruled out.

6. ORBIT runs discussed in this work assume zero electrostatic potential. TRANSP runs indicate an on-axis value of $U_0 \approx 3.5$ keV, which is significantly lower than the typical NB ion energies of interest. In general, however, potential needs to be included in the simulations as it can reach values of $20 - 40$ keV near the axis. For large amplitude modes that significantly distort the background magnetic field, even a small value of the potential can affect the simulation results, hence the computation of the kick probabilities. The electrostatic potential is introduced in ORBIT as a flux function, $U = U(\Psi_{pol})$, where Ψ_{pol} is the *unperturbed* poloidal flux. For large perturbations with $\delta B/B \sim O(0.1)$, the potential can be expected to equilibrate along the *perturbed* magnetic field lines due to the large mobility of thermal electrons (attached to the field lines). As a consequence, the potential acquires new dependencies $U \sim exp[i(n\zeta - m\theta - \omega t)]$ that are not presently included in the code. The effects of neglecting the correct dependencies propagate to the equations of motion and therefore to the computed ΔE, ΔP_ζ kicks. This inconsistency can results in discrepancies between ORBIT and TRANSP/NUBEAM results, as demonstrated by a larger disagreement observed for the case analyzed here if a finite electrostatic potential is used in ORBIT to compute the transport probability.

VI. CONCLUSIONS

A framework that enables quantitative modeling of energetic particle transport by sawteeth has been developed. The framework combines several elements from previous works into a single

workflow, implemented in the ORBIT particle-following code. Radial mode structure of the instability and its peak amplitude are computed internally, if no input is supplied from MHD codes or experimental data. Initial tests based on a NSTX-U discharge show reasonable agreement between modeled and experimental changes in thermal plasma profiles, thus giving confidence on the estimated peak mode amplitude. The ORBIT implementation includes resonant EP transport by the time-dependent internal kink evolution, and a simplified treatment of non-resonant transport caused by the sudden decay of the mode amplitude.

ORBIT results for single time-slice analysis can be transferred to TRANSP for time-dependent integrated modeling of full discharges. An initial benchmark between ORBIT results for the perturbed EP distribution function and TRANSP shows quantitative agreement in terms of EP radial density, although the fine structure of the EP distribution differs, especially for trapped fast ions. Most likely, the main cause of discrepancy for this work is due to neglecting sources, sinks and collisional processes such as scattering and slowing down in ORBIT. More generally, larger discrepancies can also be expected because of the approximate treatment of the background electrostatic potential in ORBIT for large amplitude perturbations.

More validation work is planned to compare ORBIT and TRANSP results with experimental data, including data from the coming JET DT campaign with multi-species plasmas that include NB ions (D and T) and fusion products. In fact, differences between results from over-simplified fast ion transport models and physics-based models are even more relevant for complex scenarios, such as those involving several species of fast ions originating from NB injection, RF acceleration of thermal/fast ions and fusion products [56][51]. The validation of the framework discussed in this work will benefit from additional recent improvements to the ORBIT code, such as the inclusion of a synthetic fast ion loss detector that simulates the response of the Faraday cups array installed on JET [57].

Future work includes two main improvements. First, the capability of species-dependent transport matrices will be implemented in NUBEAM. This is critical to properly account for the potentially different response of species with different charge and mass to the perturbation, as required for fusion plasmas that include significant fractions of D, T and fusion products (including alphas). Second, the possibility of including the ORBIT calculation of the transport matrices *within* a TRANSP simulation is being explored. This feature would enable more self-consistent simulations of discharges with varying heating schemes, e.g. changing from NBI-only to NBI+RF, which often results in macroscopic variations of the sawtooth parameters (sawtooth period, location of $q = 1$ surface, peak mode amplitude) during a discharge [56][51]. Updated results will be presented in

future publications.

Acknowledgments

The NSTX-U Team is gratefully acknowledged for their support in all experimental aspects of the research presented in this work. This manuscript has been authored by Princeton University and is based upon work supported by the U.S. Department of Energy, Office of Science, Office of Fusion Energy Sciences, under Contract Numbers DE-AC02-09CH11466 with the U.S. Department of Energy. NSTX/NSTX-U data can be found following the links from http://arks.princeton.edu/ark:/88435/dsp018p58pg29j. MV is supported in part by the Swiss National Science Foundation.

---

[1] S. Von Goeler, W. Stodiek, and N. Sauthoff, Phys. Rev. Lett. **33**, 1201 (1974).

[2] B. C. Stratton, R. J. Fonck, G. R. McKee, R. V. Budny, Z. Chang, F. Wising, and A. Odblom, Nucl. Fusion **36**, 1586 (1996).

[3] V. Igochine, O. Dumbrajs, H. Zohm, A. Flaws, and the ASDEX Upgrade Team, Nucl. Fusion **47**, 23 (2007).

[4] I. T. Chapman, Plasma Phys. Control. Fusion **53**, 013001 (2011).

[5] W. W. Heidbrink and B. S. Victor, Phys. Plasmas **27**, 080701 (2020).

[6] B. Kadomtsev, Soviet Journal of Plasma Physics **1**, 710 (1975).

[7] F. Porcelli, D. Boucher, and M. N. Rosenbluth, Plasma Phys. Control. Fusion **38**, 2163 (1996).

[8] N. N. Gorelenkov, R. V. Budny, H. H. Duong, R. K. Fisher, S. S. Medley, M. P. Petrov, and M. H. Redi, Nucl. Fusion **37**, 1053 (1997).

[9] Y. Kolesnichenko, V. V. Lutsenko, R. B. White, and Y. Yakovenko, Nucl. Fusion **40**, 1325 (2000).

[10] W. Shen, G. Y. Fu, Z. M. Sheng, J. A. Breslau, and F. Wang, Phys. Plasmas **21**, 092514 (2014).

[11] Y. B. Nam, J. S. Ko, G. H. Choe, Y. Bae, M. J. Choi, W. Lee, G. S. Yun, S. Jardin, and H. K. Park, Nuclear Fusion **58**, 066009 (2018).

[12] S. C. Jardin, I. Krebs, and N. Ferraro, Phys. Plasmas **27**, 032509 (2020).

[13] J. Breslau, M. Gorelenkova, F. M. Poli, J. Sachdev, and X. Yuan, [Computer Software] https://doi.org/10.11578/dc.20180627.4 (2018).

[14] Y. Kolesnichenko, V. V. Lutsenko, and Y. Yakovenko, Phys. Plasmas **4**, 2544 (1997).

[15] Y. Kolesnichenko, V. V. Lutsenko, R. B. White, and Y. Yakovenko, Phys. Plasmas **5**, 2963 (1998).

[16] Y. Zhao and R. B. White, Phys. Plasmas **4**, 1103 (1997).

[17] M. Cecconello, A. Sperduti, and the MAST team, Plasma Phys. Control. Fusion **60**, 055008 (2018).

[18] S. Bernabei, M. G. Bell, R. Budny, D. Darrow, E. D. Fredrickson, N. Gorelenkov, J. C. Hosea, R. Majeski, E. Mazzucato, R. Nazikian, C. K. Phillips, J. H. Rogers, G. Schilling, R. White, J. R. Wilson, F. Zonca, and S. Zweben, Phys. Plasmas **6**, 1880 (1999).

[19] C. C. Hegna and J. D. Callen, Phys. Plasmas **4**, 2940 (1997).

[20] C. M. Muscatello, B. A. Grierson, R. W. Harvey, W. W. Heidbrink, D. C. Pace, and M. VanZeeland, Nucl. Fusion **52**, 103022 (2012).

[21] M. Weiland, R. Bilato, B. Geiger, P. A. Schneider, G. Tardini, M. Garcia-Munoz, F. Ryter, M. Salewski, H. Zohm, and the ASDEX Upgrade Team and the EUROfusion MST1 team, Nucl. Fusion **57**, 116058 (2017).

[22] D. Liu, W. W. Heidbrink, M. Podestà, G. Z. Hao, D. S. Darrow, E. D. Fredrickson, and D. Kim, Nucl. Fusion **58**, 082028 (2018).

[23] D. Kim, M. Podestà, D. Liu, G. Hao, and F. M. Poli, Nucl. Fusion **59**, 086007 (2019).

[24] A. R. Jackson, A. S. Jacobsen, K. G. McClements, C. A. Michael, and M. Cecconello, Nucl. Fusion **60**, 126035 (2020).

[25] J. E. Menard, S. Gerhardt, M. Bell, J. Bialek, A. Brooks, J. Canik, J. Chrzanowski, M. Denault, L. Dudek, D. A. Gates, N. Gorelenkov, W. Guttenfelder, R. Hatcher, J. Hosea, R. Kaita, S. Kaye, C. Kessel, E. Kolemen, H. Kugel, R. Maingi, M. Mardenfeld, D. Mueller, B. Nelson, C. Neumeyer, M. Ono, E. Perry, R. Ramakrishnan, R. Raman, Y. Ren, S. Sabbagh, M. Smith, V. Soukhanovskii, T. Stevenson, R. Strykowsky, D. Stutman, G. Taylor, P. Titus, K. Tresemer, K. Tritz, M. Viola, M. Williams, R. Woolley, H. Yuh, H. Zhang, Y. Zhai, A. Zolfaghari, and NSTX Team, Nucl. Fusion **52**, 083015 (2012).

[26] Y. Kolesnichenko, V. V. Lutsenko, R. B. White, and Y. Yakovenko, Phys. Plasmas **11**, 5302 (2004).

[27] R. B. White and M. S. Chance, Phys. Fluids **27**, 2455 (1984).

[28] R. J. Hawryluk, in Physics of Plasmas Close to Thermonuclear Conditions (CEC, Brussels, 1980).

[29] R. J. Goldston, D. C. McCune, H. H. Towner, S. L. Davis, R. J. Hawryluk, and G. L. Schmidt, J. Comput. Phys. **43**, 61 (1981).

[30] A. Pankin, D. McCune, R. Andre, G. Bateman, and A. Kritz, Computer Physics Communication **159**, 157 (2004).

[31] W. W. Heidbrink, D. Liu, Y. Luo, E. Ruskov, and B. Geiger, Commun. Comput. Phys. **10**, 716 (2011).

[32] M. Podestà, M. Gorelenkova, and R. B. White, Plasma Phys. Control. Fusion **56**, 055003 (2014).

[33] M. Podestà, M. Gorelenkova, N. N. Gorelenkov, and R. B. White, Plasma Phys. Control. Fusion **59**, 095008 (2017).

[34] L. Lao, Nucl. Fusion **25**, 1611 (1985).

[35] B. P. LeBlanc, R. E. Bell, D. W. Johnson, D. E. Hoffman, D. C. Long, and R. W. Palladino, Rev. Sci. Instr. **74**, 1659 (2002).

[36] B. P. LeBlanc, Rev. Sci. Instr. **79**, 10E737 (2008).

[37] R. E. Bell, Phys. Plasmas , accepted for publication (2010).

[38] R. B. White, R. J. Goldston, K. McGuire, A. H. Boozer, D. A. Monticello, and W. Park, **26**, 2958 (1983).

[39] R. B. White, N. N. Gorelenkov, W. W. Heidbrink, and M. A. V. Zeeland, Plasma Phys. Control. Fusion **52**, 045012 (2010).

[40] R. B. White, Commun. Nonlinear Sci. Numer. Simulat. **17**, 2200 (2012).

[41] E. M. Carolipio, W. W. Heidbrink, C. B. Forest, and R. B. White, Nucl. Fusion **42**, 853 (2002).

[42] L. Bardóczi, M. Podestà, W. W. Heidbrink, and M. A. Van Zeeland, Plasma Phys. Control. Fusion **61**, 055012 (2019).

[43] J. Yang, M. Podestà, and E. D. Fredrickson, Plasma Phys. Control. Fusion **63**, 045003 (2021).

[44] D. Kim, M. Podestà, D. Liu, and F. M. Poli, Nucl. Fusion **58**, 082029 (2018).

[45] R. B. White, The theory of toroidally confined plasmas, 2nd ed. (Imperial College Press, London, UK, 2006).

[46] C. Z. Cheng, Phys. Rep. 211 **1** (1992).

[47] R. B. White, Phys. Plasmas **20**, 022105 (2013).

[48] N. N. Gorelenkov, A. Gondhalekar, A. A. Korotkov, S. E. Sharapov, D. Testa, and Contributors to the EFDA-JET Workprogramme, Phys. Plasmas **10**, 713 (2003).

[49] R. Farengo et al., Nucl. Fusion **53**, 043012 (2013).

[50] F. Porcelli, Plasma Phys. Control. Fusion **33**, 1601 (1991).

[51] A. A. Teplukhina, M. Podestà, F. M. Poli, G. Szepesi, Y. O. Kazakov, P. J. Bonofiglo, M. Gorelenkova, M. Nocente, J. Ongena, Z. Stancar, and JET contributors, Nucl. Fusion (submitted, 2021).

[52] M. Vallar, M. Podestà, M. Baquero-Ruiz, P. J. Bonofiglio, A. N. Karpushov, A. Merle, D. Mikitchuk, O. Sauter, and L. Stipani, Plasma Phys. Control. Fusion (submitted, 2021).

[53] S. Bernabei, M. G. Bell, R. Budny, D. Darrow, E. D. Fredrickson, N. Gorelenkov, J. C. Hosea, R. Majeski, E. Mazzucato, R. Nazikian, C. K. Phillips, J. H. Rogers, G. Schilling, R. White, J. R. Wilson, F. Zonca, and S. Zweben, Phys. Plasmas **6**, 1880 (1999).

[54] G. Y. Fu and C. Z. Cheng, Phys. Fluids B **4**, 3722 (1992).

[55] N. N. Gorelenkov, C. Z. Cheng, and G. Y. Fu, Phys. Plasmas **6**, 2802 (1999).

[56] A. A. Teplukhina, M. Podestà, F. M. Poli, N. Bertelli, M. Gorelenkova, Y. O. Kazakov, and JET contributors, in IAEA Fusion Energy Conference (virtual meeting, 2021).

[57] P. J. Bonofiglo, V. Kiptily, A. Horton, P. Beaumont, R. Ellis, F. E. Cecil, M. Podestà, and JET Contributors, Rev. Sci. Instrum. **92**, 043553 (2021).